

# Pencil Powered Faradaic Electrode for Lithium-Ion Capacitors with High Energy and Wide Temperature Operation

Madhusoodhanan Lathika Divya,<sup>[a]</sup> Yun-Sung Lee,<sup>\*[b]</sup> and Vanchiappan Aravindan<sup>\*[a]</sup>

Lithium-ion capacitors (LICs) are considered next-generation energy storage devices that combine the goodness of both Li-ion batteries and electric double-layer capacitors. In this work, LIC is assembled with electrochemically pre-lithiated ( $\text{LiC}_6$ ) pencil graphite (PG, 1B&4H grades) as anode and activated carbon (AC) as the cathode. PG grades, naturally available graphite silica composite materials, are characterized, and the electrochemical performance is studied in half-cell assembly for 14 grades. PG grades in the middle of the hardness scale demonstrated better electrochemical activity than the end compositions, representing the involvement of graphite and silica's role in overall performance. However, it is observed that

$\text{SiO}_2$ /clay component in PG material is to provide only mechanical support to the system considering the inactiveness of  $\text{SiO}_2$  towards Li storage. The assembled LICs (AC/PG 1B LIC) & (AC/PG 4B LIC) delivered maximum energy density of  $\sim 172$  &  $\sim 162 \text{ Wh kg}^{-1}$ , respectively, with long-term stability under balanced mass loading conditions. Besides ambient temperature, the LICs exhibited stable performance at low ( $-5$  and  $10^\circ\text{C}$ ) and high-temperature ( $50^\circ\text{C}$ ) conditions. The outstanding electrochemical performance of PG material in LIC assembly indicates the choice of pencil's aptness in energy storage devices.

## Introduction

Energy storage systems (ESS) play a critical role in promoting clean energy by considering the potential of renewable resources.<sup>[1–3]</sup> Diverse energy storage options are available; among them, electrochemical energy storage (EES) systems are significant in sustainable energy development.<sup>[4,5]</sup> Research on EES mainly focused on finding new energy storage materials and understanding their suitability.<sup>[6]</sup> Lithium-ion batteries (LIBs) and electrical double-layer capacitors (EDLCs) are commonly used for high-energy and high-power applications and are treated as the most popular ESS today. LIBs can store more energy and have applications ranging from consumer electronics to electric vehicles (EVs). EV applications have strict technical necessities such as cycle life ( $\geq 1000$  cycles), calendar life of nearly ten years, high and low-temperature stability, and cost. Thus, challenges are lasting for the LIBs for use in automotive applications, mainly in terms of cycle life, cost, safety, and fast charging capability.<sup>[7]</sup> EDLCs can provide high power and prolonged cycle life with low energy storage capability. Lithium-ion capacitors (LICs) are hybrid energy

storage devices merging the benefits of both LIBs and EDLCs.<sup>[8–12]</sup> They have recently gained much attention for their increased energy density, power density, safety, and long cycle life.<sup>[13–16]</sup> Hence, they can be considered an efficient energy storage system for the renewable future.<sup>[17,18]</sup>

Among the LICs explored, dual-carbon-based LICs combine high surface area activated carbon (AC) as cathode and pre-lithiated Li-ion intercalating carbon (mainly graphite or hard carbon) as the anode.<sup>[19–21]</sup> Graphite has a layered structure, nearly flat Li-intercalation/de-intercalation profile, a low redox potential ( $< 0.15 \text{ V vs. Li/Li}^+$ ), and a theoretical capacity of  $372 \text{ mAh g}^{-1}$  for  $\text{LiC}_6$  formation.<sup>[22]</sup> Several reports are available on assembling LICs with graphite anode and AC cathode. Khomonko et al. reported LIC assembly with commercial graphite anode and AC cathode in 2008.<sup>[23]</sup> The assembled device showed long-term stability and could deliver maximum energy and power density of  $103.8 \text{ Wh kg}^{-1}$  and  $\sim 10 \text{ kW kg}^{-1}$ , respectively. In 2011, Sivakumar and co-workers studied the performance of ball-milled graphite anode in LIC devices.<sup>[24]</sup> They reported that three-hour ball-milled graphite could give better performance in LIC assembly for higher current rates and long-term stability than a pristine one. In 2017, Cai et al. framed a LIC prototype with pre-lithiated MWCNTs/graphite composite as anode and AC cathode.<sup>[25]</sup> The device could deliver maximum energy and power density values of  $96 \text{ Wh kg}^{-1}$  and  $10.1 \text{ kW kg}^{-1}$ , respectively, with 86% capacity retention after 3000 cycles. Our group recently reported a LIC assembly with pre-lithiated recovered graphite (RG) from spent LIB as the anode.<sup>[26]</sup> The thus formed device could deliver a higher energy density of  $185.54 \text{ Wh kg}^{-1}$  with 75% capacity retention after 2000 charge-discharge cycles. We also attempted a new form of LIC by coupling pre-lithiated  $\text{SnO}_2$ @graphite nanocomposite

[a] M. L. Divya, Dr. V. Aravindan  
Department of Chemistry  
Indian Institute of Science Education and Research (IISER)  
Tirupati 517507, India  
E-mail: aravind\_van@yahoo.com

[b] Prof. Y.-S. Lee  
School of Chemical Engineering  
Chonnam National University  
Gwangju, 61186, Republic of Korea  
E-mail: leeys@chonnam.ac.kr

 Supporting information for this article is available on the WWW under  
<https://doi.org/10.1002/batt.202200214>

as the anode and AC as the cathode.<sup>[27]</sup> The assembled LIC with 25% SnO<sub>2</sub> and 75% graphite (Li<sub>x</sub>Sn & LiC<sub>6</sub>) composite as anode could deliver an energy density of 172.33 Wh kg<sup>-1</sup>. This study also showed the possibility of combining alloy-type materials into intercalation-based anodes to improve the dual carbon electrochemical device in terms of power capability.

Pencil lead is composed of graphite with clay particles, mainly containing SiO<sub>2</sub> and small amounts of other metal oxides. And hence, pencil graphite (PG) material can be considered a naturally available graphite-silicon composite with electrical conductivity. The material displays slightly different properties than pure graphite due to clay particles. PG has H (hardness) and B (blackness) grades based on the graphite to clay ratio. Graphite provides blackness, and clay offers hardness to the PG material. Based on the literature data, the approximate composition of PG grades is listed in Table S1.<sup>[28]</sup> Clay in the pencil graphite is none other than silica, SiO<sub>2</sub>, which is one of the amplest materials on earth. When used in Li-based electrochemical systems, it usually does not react with Li due to a stable oxide layer on the surface of the material. But SiO<sub>2</sub> can act as a buffering medium to improve the mechanical stability during cycling.<sup>[29]</sup> In 2016, Park et al. designed a simple binder-free pencil trace electrode (4B) on a ground Cu substrate and considered that as an anode material for LIB applications.<sup>[30]</sup> They stated that Li<sub>x</sub>Si alloys were formed by the interaction between Li<sup>+</sup> and active Si, which was produced due to electrochemical reduction of nano SiO<sub>2</sub> in the clay particles present between multi-layered graphite. Navratil et al. reported that there is high content of sp<sup>3</sup> hybridized carbon with a small degree of surface oxidation, demonstrating the presence of silicon monoxide (SiO) in excess over silicon dioxide (SiO<sub>2</sub>) on the surface of PG material.<sup>[31]</sup> In this work, we have made a preliminary study on the electrochemical performance of all the 14 grades of PG material (graphite clay composites) to understand the effect of graphite-clay composition on charge-storage applications. Half-cell performance revealed that SiO<sub>2</sub>/clay component in PG material has only passive role that is to provide mechanical support to the system due to inactiveness of SiO<sub>2</sub> towards reversible Li storage. After preliminary studies, PG 1B and 4H grades were considered to use as anode material (after pre-lithiation) for LIC assembly by pairing with AC cathode under the balanced mass loading conditions. In addition to ambient temperature performance, the high and low-temperature performance of assembled LICs were also investigated and explained in detail.

## Results and Discussion

The phase purity and crystallinity of PG samples were studied using powder XRD patterns, Figure S1. The sharp diffraction peak around  $2\theta=26^\circ$  (002) and a small peak at  $55^\circ$  (004) divulge the crystalline nature of all the PG grades and indicate the presence of natural graphite.<sup>[32]</sup> The intensities of peaks corresponding to the presence of clay in the PG material vary concerning the composition of PG grades and are clearly visible for 4H and 6H. Figure 1(a) illustrates the XRD pattern of PG 1B

and 4H grades along with standard graphite (C), PDF 00-023-0064, and quartz (SiO<sub>2</sub>), PDF 01-083-0539. This clearly shows that PG material is a composite of graphite and silica.<sup>[30]</sup> Figure 1(b) displays Raman spectra of the PG 1B and 4H grades, which show peaks corresponding to defect (D), graphitic (G), and 2D (G\*) bands positioned at  $\sim 1350$ ,  $\sim 1580$ , and  $\sim 2720$  cm<sup>-1</sup>, respectively.<sup>[30,33-35]</sup> The values of  $I_D/I_G$  were obtained as 0.66 and 0.89 for PG 1B and 4H grades, respectively. These values certainly help to estimate the degree of defects or disorders in the graphitic structure. Moreover, this shows that defects are growing with increased clay content in the pencil graphite. Besides, the presence of a 2D band with  $I_{2D}/I_G < 1$  indicates layered graphitic lattices.<sup>[32,36,37]</sup> The average size of graphitic crystallites in the PG materials can be calculated using Tuinstra and Koenig correlation such that  $I_0/I_G = A/\lambda_a$ ; where La and A represents crystallite size (nm) and laser excitation energy (515 nm laser source), respectively.<sup>[33,37,38]</sup> The graphitic crystallite sizes of PG 1B and 4H were calculated as 25.57 and 18.96 nm, respectively, with a decrease in crystallite size with increased clay content.<sup>[39]</sup>

The elemental composition on the surface of PG materials was determined via XPS spectra, Figure 1(c). The raw spectrum revealed that the material surface contains carbon, oxygen, and a trace amount of silicon. Quantitative analysis showed that PG 1B and PG 4H contain 82.22% and 79.12% carbon, and 17.78% and 20.88% oxygen, respectively, pointing that Si atoms are not present on the material surface or they are in low atomic percentages close to that of the detection limit. Inaccurate elemental composition from XPS is possible due to factors like (1) adventitious carbon contamination, (2) inability to detect H atoms, and dependency on the depth of atom present in the sample.<sup>[40,41]</sup> A thorough assessment of individual peaks is given in supplementary data, Figure S2. The deconvoluted C1s spectrum of both the materials disclosed that the majority of carbon is in the form of graphite (C-C,  $\sim 284.6$  eV). The two minor components are C-OH ( $\sim 286$  eV) and O-C=O ( $\sim 288$  eV), in which the intensity of the first one is more in PG 1B and the second one is more in PG 4H.<sup>[42]</sup> O 1s deconvoluted peak position and intensities are slightly varying for PG 1B and PG 4H. We could observe a shift in peak position towards higher binding energy and the change in peak intensities corresponding to more oxidation states of PG 4H compared to PG 1B. In addition, peaks due to water and organic contamination components may overlay directly with the SiO<sub>2</sub> peak. The position of Si 2p and Si 2s peaks ( $\sim 103$  and  $\sim 152$  eV) was consistent with that of siloxanes.<sup>[43-45]</sup> Also, the presence of impurity elements (from clay and binder) can be ensured by the occurrence of minor peaks between 0-200 eV. Figure S3 displays the energy-dispersive X-ray spectra (EDS) of two PG materials with normalized peak intensities. The relative amount of graphite (C) to clay content (O, Al, Si, and S) and binder can be analyzed from the spectrum, and it shows that PG 4H contains a higher portion of clay and binder in comparison with PG 1B.<sup>[46]</sup> The TGA analysis of PG materials (initial mass  $\sim 16$  mg) in the presence of oxygen burns carbon fractions (graphite) and leaves an inorganic residue. Figure 1(d) confirmed that there is a direct relationship between PG grade and

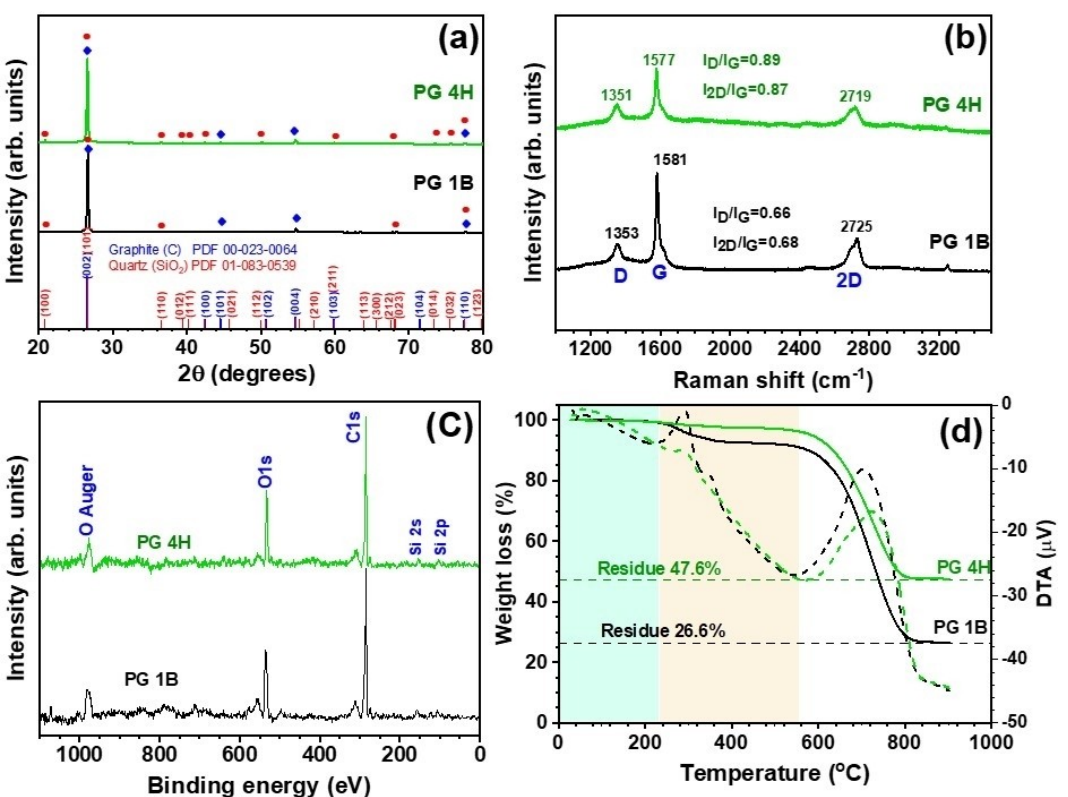


Figure 1. a) XRD patterns, b) Raman spectra, c) XPS spectra, and d) TGA&DTA curves of PG 1B and 4H materials.

the residue lasting at the end of 900 °C such that the amount of residue rises with increasing hardness of pencil grade, PG 4H > PG 1B.<sup>[45]</sup> Besides, differential thermal analysis (DTA) of the PG materials displays peaks that match the temperatures where thermal events happen.<sup>[47]</sup>

The field emission scanning electron microscopy (FE-SEM) and high-resolution transmission electron microscopy (HR-TEM) pictures of PG materials are shown in Figure 2. FE-SEM images show stacked graphene flakes of irregular shape and a few microns in size with surface heterogeneity due to the presence of clay, Figure 2(a-d).<sup>[33]</sup> Moreover, increased clay content in PG 4H in comparison with PG 1B can be seen from the reduced size of graphene flakes with increased surface heterogeneity. Apparently, the inhomogeneity of the SiO<sub>2</sub> is evident from the FE-SEM pictures, which eventually leads to the variation in the electrochemical performance. HR-TEM images, Figure 2(e and f), demonstrate the long-range ordering of graphitic domains in the form of graphene planes with an interplanar spacing of 0.343 and 0.354 nm for PG 1B and PG 4H materials, respectively. The small dark patches like possible contamination on the surface of the graphite plane observed on the HR-TEM images characterize the clay part (SiO<sub>2</sub>) of PG material, Figure S4. In addition, Figure 2(g and h) in the inset shows the selected area electron diffraction (SAED) pattern with concentric bright spots with a dark ring-like design, illustrating the polycrystalline nature of PG material having diffraction planes corresponding to planes of graphite and SiO<sub>2</sub>, indicating the composite nature of the material. Figure S5 shows the EDS

elemental mapping of PG materials at low magnification, demonstrating the presence of elements like C and O.

The electrochemical performance of PG materials was analyzed in half-cell configuration with Li metal counter/reference electrode in CR 2016 coin-cell assembly. The initial screening of PG materials was carried out by GCD technique at a current density of 100 mA g<sup>-1</sup>, Figure S6(a), and EIS measurement within the frequency range of 10 kHz to 1 Hz, Figure S6(b). The GCD analysis showed that all the PG grade-based electrodes could deliver a second discharge capacity greater than 230 mAh g<sup>-1</sup> with initial Coulombic efficiency (CE) of ~60%. It was observed that the middle-grade PG materials (HB, 1B, 2B & 3B) could deliver maximum discharge capacity (350–370 mAh g<sup>-1</sup>) in comparison with harder (H) and softer (B) end. Further, it was noticed that the H grade materials (2H, 4H & 6H) exhibit slightly different charge-discharge profiles in comparison with other grades indicating the presence of higher clay content, with PG 4H displaying better performance than the other two. The EIS spectrum ensures the electronic conductivity of the materials, and it includes a semicircle in the high to medium frequency region and an angled line in the low-frequency area representing the Li-storage kinetics. H (hardness) and B (blackness) are two different scales in which an increase in clay content can increase the hardness while the increase in graphitic content can increase the blackness. For H grade pencils, it is observed that resistance increases as the hardness of the pencil increase due to increased clay content. But for B grade pencils, a decrease in resistance should be

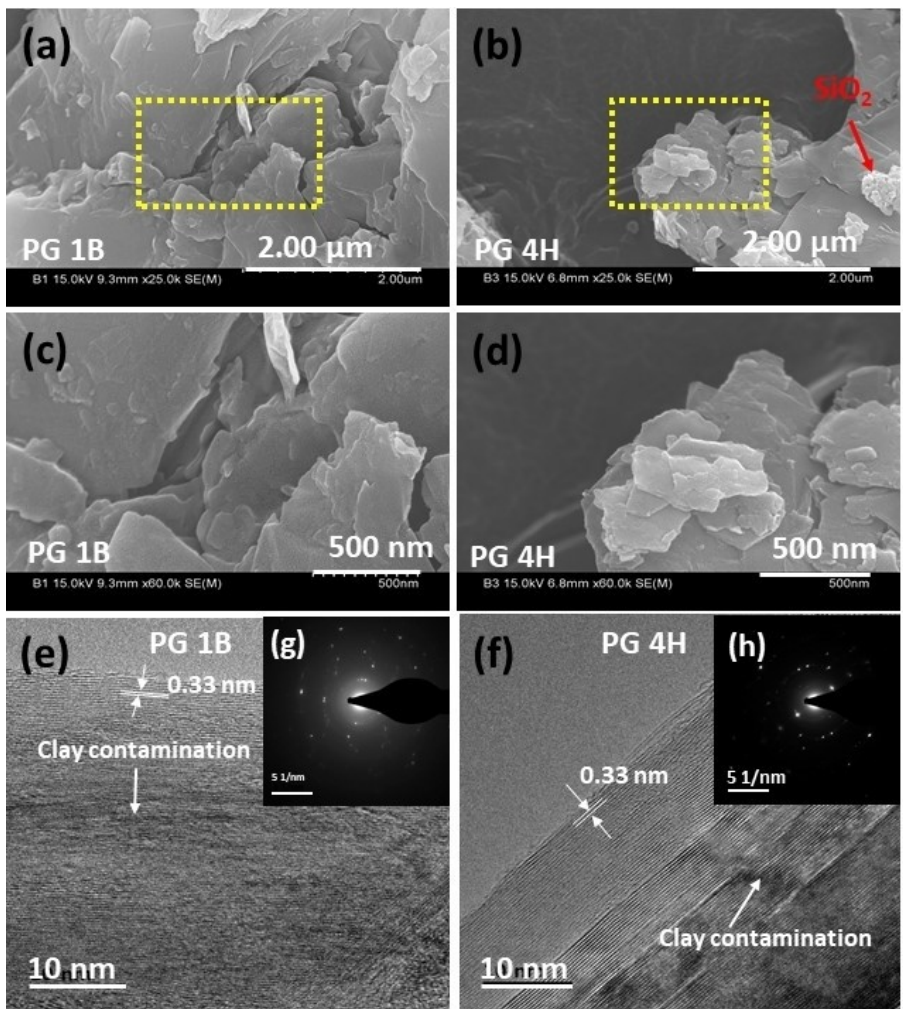


**Figure 2.** FE-SEM, HR-TEM and SAED patterns of PG materials: a and b) low magnification FE-SEM images, c and d) high magnification FE-SEM images, e and f) HR-TEM images, and g and h) SAED patterns (inset).

observed with an increase in graphitic content. Unlike the H grade, the B grade showed an irregular pattern in resistance with an increase in graphitic scale. By considering the difference in charge-discharge profile and graphite clay composition, PG 1B and 4H grade materials were considered for further analysis and hybrid cell assembly.

Figure 3(a) illustrates the GCD profiles (1<sup>st</sup> and 2<sup>nd</sup> cycle) of PG 1B and 4H material at a current density of 100 mA g<sup>-1</sup>. They could deliver initial discharge capacities of ~520 (PG 1B) and 554 mAh g<sup>-1</sup> (PG 4H) with 62 and 66% of CE, respectively. And corresponding second discharge capacity values were obtained as 357 and 353 mAh g<sup>-1</sup>. The first discharge profiles of PG 1B and 4H have been plotted along with commercial graphite and the two extreme cases of PG grades (12B and 6H) to analyze the contribution of capacity from graphite and clay parts. Figure S7(a) gives a comparison of sloping and flat voltage plateaus in the first lithiation process. It is clear that the flat plateau at 0.3 to 0.5 V vs. Li<sup>+</sup>/Li is due to the partial decomposition of the wax component in the pencil. Figure S7(b) demonstrates the second charge-discharge profile of PG 1B, 4H, 12B, and 6H against commercial graphite. Fig-

ure S7(c) shows the good cyclability of all the four PG materials tested at a current density of 100 mA g<sup>-1</sup>. PG 1B shows CE of ~96% at the end of 80 cycles, whereas the other three grades exhibit slightly higher CE (~100%–110%), indicating a small degree of structural interference due to the presence of clay content. Figure 3(b) shows that after 100 charge-discharge cycles at 100 mA g<sup>-1</sup>, the PG 1B and 4H maintain ~76% and 68% of their second discharge capacity values. Both PG 1B and 4H were chosen for further studies in the practical assembly with the active counter electrode.

The electrochemical performances of PG materials were also examined by cyclic voltammetry (CV). Figure 3(c and d) illustrates a cyclic voltammogram (1<sup>st</sup>, 2<sup>nd</sup>, and 3<sup>rd</sup> cycle) of PG 4H and 1B between the voltage window of 0.005–2 V vs. Li<sup>+</sup>/Li tested at a scan rate of 0.1 mV s<sup>-1</sup>. The irreversible cathodic peak positioned between 0.6–0.7 V vs. Li<sup>+</sup>/Li in the first cycle corresponds to electrolyte decomposition and the subsequent development of the solid electrolyte interface (SEI) layer on the graphite. The absence of this peak in the subsequent cycles indicates stable SEI layer formation. The distinct cathodic peak observed between 0.3–0.5 V vs. Li<sup>+</sup>/Li in the first cycle is

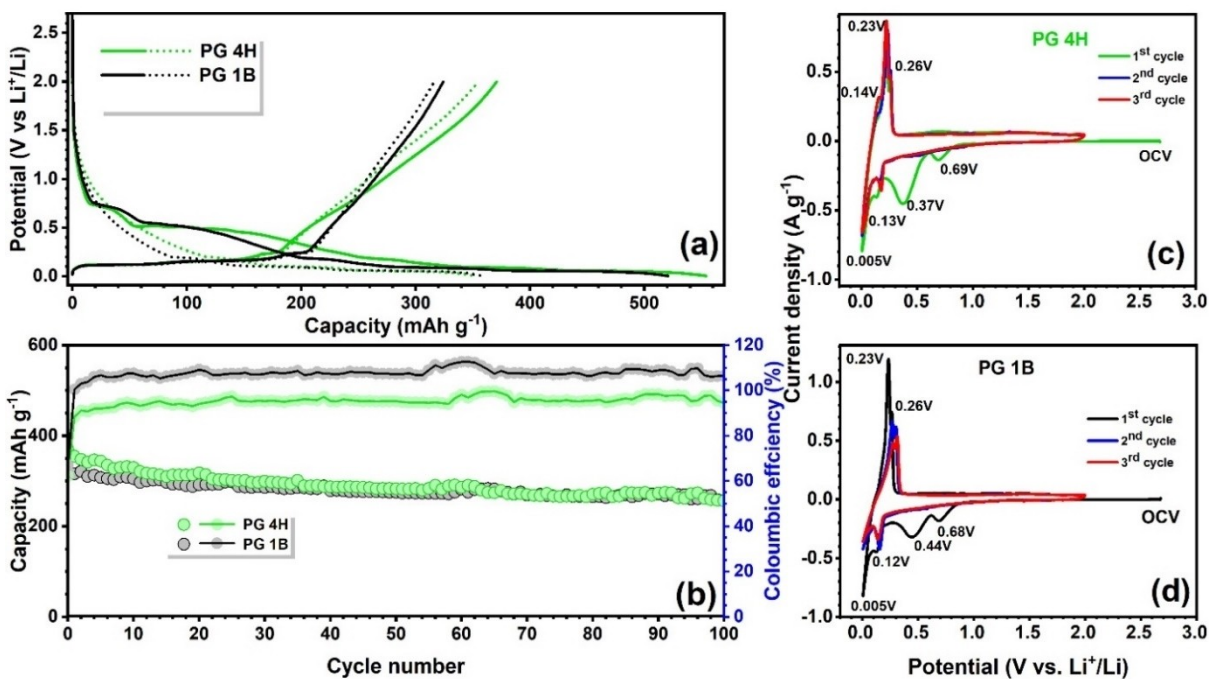


**Figure 3.** Electrochemical performance of PG materials: a) Charge-discharge profiles for the first two cycles at a current density of  $100 \text{ mA g}^{-1}$  in the potential window from  $0.005\text{--}2 \text{ V vs. Li}^+/\text{Li}$ , b) cycling performance and coulombic efficiency at a current density of  $100 \text{ mA g}^{-1}$ , and c and d) Cyclic voltametric profiles of first three cycles of PG electrodes recorded at a scan rate of  $0.1 \text{ mV s}^{-1}$ .

attributed to the partial reduction of wax. This irreversible reaction and SEI layer formation gulp much Li, which is an important reason for irreversible capacity in the first lithiation step. At the same time, we could not notice any reversible reactivity of  $\text{SiO}_2$ , mainly oxidation peaks. For graphite, reversible formation of  $\text{Li}_x\text{C}_6$  takes place within the potential range between  $0.2\text{--}0.005 \text{ V vs. Li}^+/\text{Li}$ . Considering the overlying voltage plateau regions of graphite ( $0.2\text{--}0.005 \text{ V vs. Li}^+/\text{Li}$ ) and Si (single gradually sloping plateau  $\sim 0.1 \text{ V vs. Li}^+/\text{Li}$ ) during lithiation, it is not easy to distinguish the role of each peak. The anodic peaks detected at  $0.23$  and  $0.26 \text{ V vs. Li}^+/\text{Li}$  correspond to Li-ion removal from the graphitic lattice of PG material. On the other hand, the de-alloying reaction of  $\text{Li}_x\text{Si}$  alloy will take place beyond  $0.45 \text{ V vs. Li}^+/\text{Li}$  for the case of Si-based derivatives. The absence of such prominent anodic peaks clearly suggests the inactiveness of  $\text{SiO}_2$ -based clay toward Li-storage/electrochemical activity. Figure S7(d-g) displays the first three cycle CV profiles of PG materials 12B, 1B, 4H, and 6H, which give a clear idea about the change in peak intensity and position concerning the PG grade. Moreover, it is noticed that the CV plots agree with GCD curves. To further explore the electrochemical behavior of PG materials, long-term cyclability at high current and rate performance was examined. As mentioned, the uneven distribution of the clay/ $\text{SiO}_2$  particles in the PG is reflected in the half-cell studies; for example, high  $\text{SiO}_2$  content (PG 4H) rendered marginally better performance than low clay content (PG 1B) (Figure 3a and b). As shown in Figure S8, PG 1B and 4H could deliver discharge capacity values of  $188$  and  $110 \text{ mAh g}^{-1}$  even after  $900$  charge-discharge cycles at a very high current rate of  $1 \text{ A g}^{-1}$  ( $\sim 2.7 \text{ C}$ ). Figure S9(a)

explains the rate capability of PG materials between  $0.05$  to  $1 \text{ A g}^{-1}$ , and it explains that the materials exhibit maximum reversible capacity at a low current density of  $100 \text{ mA g}^{-1}$ . As observed through FE-SEM analysis and galvanostatic studies, the inhomogeneity of the clay leads to a minimal deviation ( $\sim 3\%$ ) in the electrochemical performance. Figure S9(b and c) presents CV profiles of PG 1B and 4H recorded at scan rates varying from  $0.1$  to  $1 \text{ mV s}^{-1}$ . An increase in scan rates results in increased redox peak currents and a slight upsurge in oxidation-reduction peak potential interval, which implies minor polarization in PG electrodes. Figure S10 displays the Nyquist plots and corresponding fitted curves measured in a frequency range of  $10 \text{ kHz}$  to  $10 \text{ mHz}$  for PG 1B and 4H material. Inset shows the enlarged view of the high-frequency region. The electrolyte resistance and charge transfer resistance are slightly less in the case of PG 4H ( $15$  &  $100 \Omega$ ) than PG 1B ( $35$  &  $150 \Omega$ ).<sup>[48]</sup> Thus, a comparison between two different scales (H and B grade) in terms of resistance shows irregularity. But we could confirm that both the selected grades exhibit low electrochemical resistance compared to the other grades screened, indicating their suitability to use as battery type anodes. Thus, the Nyquist plots agree with PG material's rate capability and cyclic stability, along with enhanced Li-ion diffusion rate and electronic conductivity.

Thus, pencil graphite electrodes represent the co-utilization of graphite and silica ( $\text{SiO}_2$ ), which is intricate due to their differences in properties. The lithiation in graphite can be denoted by the equation,



But silica ( $\text{SiO}_2$ ) does not react with Li due to its stable oxide layer.<sup>[29,31]</sup> It was also reported that this  $\text{SiO}_2$  surface layer remains inert under lithiation owing to activation energy and overpotential essential to break the Si–O bond. Whereas  $\text{SiO}_2$  can exhibit Li reactivity in the amorphous state, the exact reaction mechanism is still not fully understood.<sup>[49,50]</sup> Some previous studies reported that silicon monoxide (SiO) or silicon suboxide ( $\text{SiO}_x$ ) dominates  $\text{SiO}_2$  on the surface of pencil graphite material. Apparently, there is a complexity in distinguishing the Li-intercalation (into graphite) and Li-alloying (with Si) potential for this particular composite during the cathodic scan. However, during the anodic scan, it is very easy to figure out that the de-alloying of  $\text{Li}_x\text{Si}$  will occur beyond  $\sim 0.3$  V vs. Li.<sup>[51–53]</sup> Therefore, in the present system, it is noticed that the capacity of the material is provided by graphite matrix, and silica imparts only stability to the system.

## Hybrid Li-ion capacitor (LIC) assembly

Hybrid LICs were assembled using PG 1B and 4H as anode and commercial AC as the cathode in 1 M  $\text{LiPF}_6$  in EC: DMC (1:1) solution. The AC cathode half-cell was tested within the potential window of 2–4.5 V vs.  $\text{Li}^+/\text{Li}$ . Figure S11(a) displays the corresponding linear GCD profiles with a second discharge capacity of  $\sim 85$ – $90$  mAh g $^{-1}$  at a current density of 100 mA g $^{-1}$ . Figure S11(b) provides superior cyclability of AC cathode for 100 cycles with boosted capacity. Figure S11(c) illustrates near rectangular-shaped CV traces indicating the capacitive nature of the material. Before the assembly of hybrid LIC, the PG anode was gathered in a half-cell configuration and subjected to two complete discharge-charge cycles followed by a final discharge (pre-lithiated). The pre-lithiated anode ( $\text{LiC}_6$ ) was combined with an AC cathode with a mass ratio of 1:4 to balance the charge, based on the equation  $Q_+ = Q_- = m_+q_+ = m_-q_-$ , where  $Q$ ,  $q$ , and  $m$  represents capacity, specific capacity, and mass of active material in the electrode, respectively. The subscripts + and – denote positive and negative electrodes, respectively. The fabricated AC/PG 1B and AC/PG 4H LICs with the same electrolyte were tested within a 1.8–4.3 V voltage window. During charging,  $\text{PF}_6^-$  ions are adsorbed on the surface of the AC cathode, and  $\text{Li}^+$ -ions are intercalated into PG material. During discharge, the desorption of  $\text{PF}_6^-$  ions and de-intercalation/de-alloying of  $\text{Li}^+$  ions occur. Figure 4(a) demonstrates the Ragone plots of assembled LICs, and it was observed that both the LICs could deliver nearly identical performances irrespective of the difference in graphite clay content in the anode. AC/PG 1B LIC could provide a maximum energy density of 172 Wh kg $^{-1}$  at a power density of 0.17 kW kg $^{-1}$ , and even at high power of 5.29 kW kg $^{-1}$ , the device exhibited 95 Wh kg $^{-1}$ . On the other hand, AC/PG 4H-based LIC could offer a maximum energy density of 162 Wh kg $^{-1}$  at a power density of 0.175 kW kg $^{-1}$ , and even at high power of 5.24 kW kg $^{-1}$  device rendered the energy density of 107 Wh kg $^{-1}$ . It is also observed

that AC/PG 1B LIC displays supremacy in energy values, and AC/PG 4H LIC demonstrates domination in the case of power, mainly at low current density values. Inset shows the GCD profiles of assembled LICs at different current rates (0.05–1.5 Ag $^{-1}$ ) at ambient conditions. Applied current values are calculated based on the total mass of active material in the positive and negative electrodes. The near-symmetrical charge-discharge curves of both the LICs represent excellent reversibility. Besides, the deviation of GCD curves from the ideal triangular shape means the hybrid charge storage mechanism of the device. Figure 4(b and c) depicts the typical CV curves of AC/PG 1B LIC and AC/PG 4H LIC at different scan rates (0.5, 1, 2, and 3 mV s $^{-1}$ ). The non-rectangular symmetric CV curves of both the LICs denote the hybrid nature of the battery-type PG electrodes and capacitive-type AC electrodes. The shape of the CV profile is slightly different for both the LICs, signifying the difference in the anode. Figure 4(d) presents the long-term cycling test of the LICs at a current density of 1 Ag $^{-1}$ . After 4000 charge-discharge cycles, AC/PG 1B LIC and AC/PG 4H LIC could retain  $\sim 96$  and  $\sim 87\%$  of initial capacity values, proving greater cyclic stability of the device.

The performance of LICs at different temperature conditions was analyzed with the support of an environmental chamber. Both the LICs could exhibit comparable and good performance at low and high-temperature conditions. At high (50°C) and low temperature ( $-5^\circ\text{C}$ ) conditions, AC/PG 1B LIC could deliver a maximum energy density of 153 and 120 Wh kg $^{-1}$ , whereas AC/PG 4H LIC could provide 161 and 121 Wh kg $^{-1}$ , Figure 5(a and b). Figure S12 displays the GCD profiles of both LICs at different temperature conditions. The deviated-linear charge-discharge profiles, even at high and low-temperature conditions, indicate the suitability of the assembled device is extremely low and high environmental conditions. The Nyquist plots of LICs at different temperature conditions, Figure S13, show an apparent change in impedance values concerning temperature. It was observed that a decrease in temperature increased electrolyte resistance and charge-transfer resistance. Also, the cyclic stability of LICs was tested at low and high-temperature conditions, and it was observed that AC/PG 1B LIC could exhibit more stability in ambient conditions, while AC/PG 4H LIC demonstrated better stability at low and high-temperature conditions Figure 5(c and d). This indicates slightly higher clay content may enhance the stability of LIC at extreme temperature conditions. The higher energy density and stability of LICs at different temperature conditions encourage PG material as active anode material for the fabrication of LICs, and even the waste pencils could be efficiently re-utilized. Besides, the higher stability of AC/PG 4H LIC at low and high-temperature conditions affirms the potential benefit of partially inactive silica particles in the graphite host matrix.

Figure 6 illustrates the performance comparison of various LICs fabricated with different types of graphitic carbon materials as battery type anodes. PG-based LICs exhibit a comparable performance such as natural graphite,<sup>[54]</sup> graphitic carbon spheres from the vegetable oil,<sup>[55]</sup> graphitic carbon fibers from the cooking oil,<sup>[56]</sup> natural plant-based hard

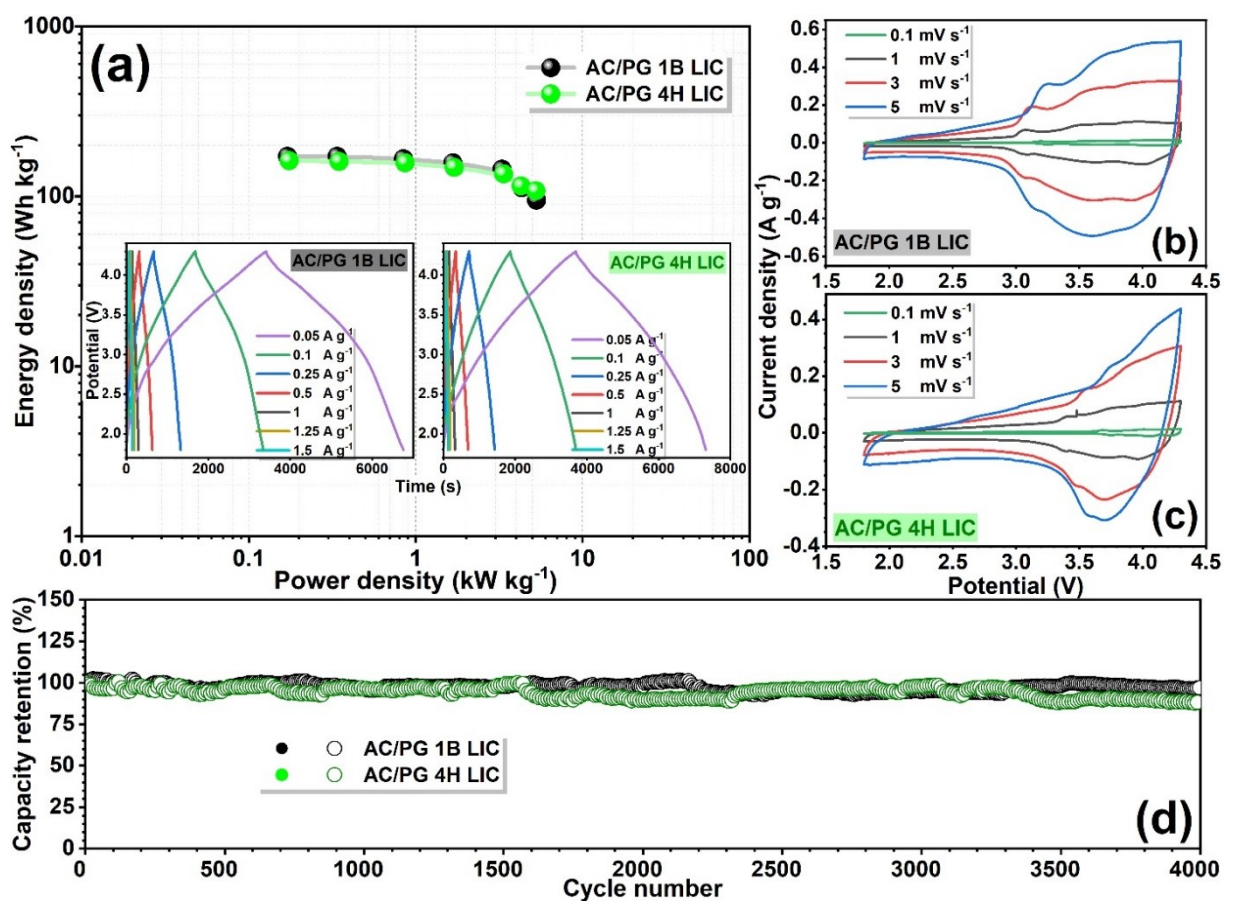


**Figure 4.** Electrochemical performance of AC/PG LICs: a) Ragone plots and galvanostatic charge-discharge profiles at diverse current rates within the voltage window of 1.8–4.3 V, b and c) CV profiles at different scan rates, and d) Long term cyclability at a current density of 1 Ag<sup>-1</sup> in the ambient temperature conditions.

carbon,<sup>[57]</sup> semi-crystalline carbon derived from *prosopis juliflora*,<sup>[58]</sup> and expanded graphite or recovered graphite from the spent LIB.<sup>[26]</sup> As of now, recovered graphite (expanded) from spent LIB is considered the best reported graphitic carbon-based insertion host, as it outperforms natural graphite. However, it is very much clear that pencil graphite also falls into one of the best battery type electrodes for the fabrication of high performance LIC configurations.

## Conclusion

In summary, PG material (1B and 4H), a naturally present graphite, clay composite, was used as active anode material to fabricate LIC for the first time. The electrochemical performance of PG materials revealed that SiO<sub>2</sub>/SiO<sub>x</sub> present in the material is not involved in reversible lithiation/de-lithiation reaction but translates the stability during the long-term cycling irrespective of the temperature conditions. The assembled LICs could provide higher energy density values of 172 (AC/PG 1B LIC) and 162 (AC/PG 4B LIC) Wh kg<sup>-1</sup> at a power density value of ~0.17 kW kg<sup>-1</sup> with long term stability and the performance is comparable with other previously reported LICs. Moreover, in the LIC assembly, increased clay content could enhance the

stability of LIC at low and high-temperature conditions. Thus, the study indicates that PG material is a promising anode material for LIC assembly with high energy, power, long term stability with a wide temperature range of operation. Moreover, this study revealed the possibility of considering the mixture of different PG grades (waste PG materials) as the active anode material for LIC assembly according to the waste-to-wealth approach.

## Experimental Section

### Sample preparation and cell assembly

Kasimir drawing pencils (14 grades-12B, 10B, 8B, 7B, 6B, 5B, 4B, 3B, 2B, 1B, HB, 2H, 4H & 6H) were purchased and used for electrode material preparation. The pencil lead of all the grades was broken into small pieces and ball-milled for 5 minutes with a 1:10 ball ratio (wt%) with a high-energy ball mill (SPEX, USA). Further, the powder obtained was ground in mortar and pestle and was used for slurry preparation. The slurry was made in the weight ratio of 80:10:10 by adding active material, conductive carbon (acetylene black), and polyvinylidene fluoride (PVDF) binder into solvent 1-methyl 2-pyrrolidone (NMP). After overnight mixing, the slurry coating was done on Cu foil with a doctor blade, then dried in the hot air oven for four hours, and pressed under a hot roll press

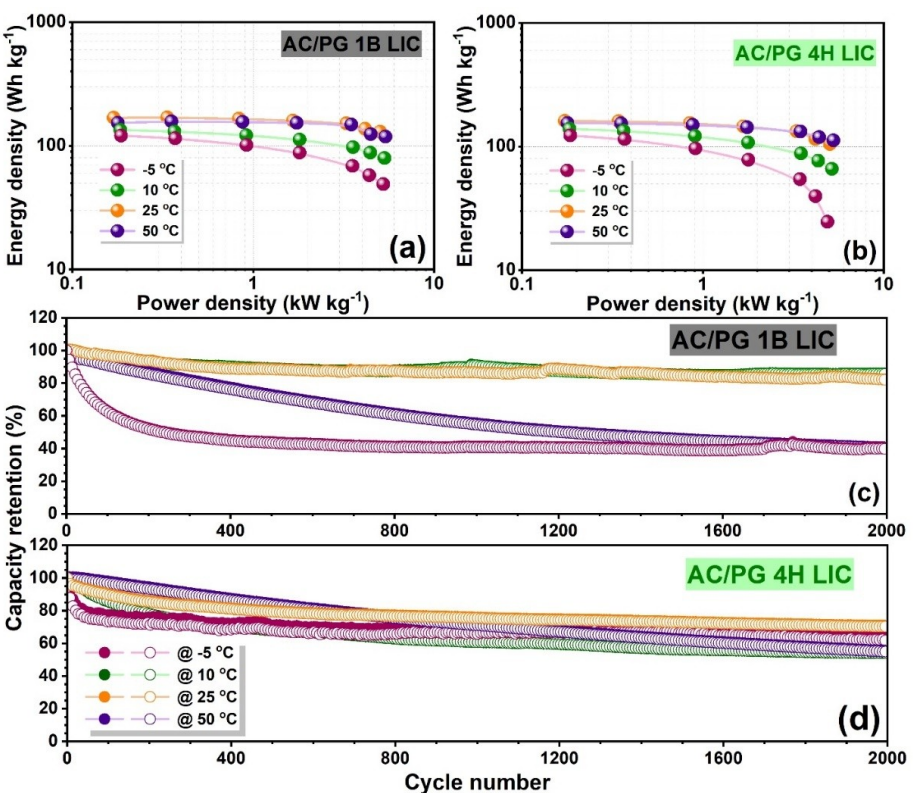


**Figure 5.** Electrochemical performance of AC/PG LICs at different temperature conditions: a and b) Ragone plots, and c and d) long term cyclability at a current density of  $1 \text{ A g}^{-1}$ .

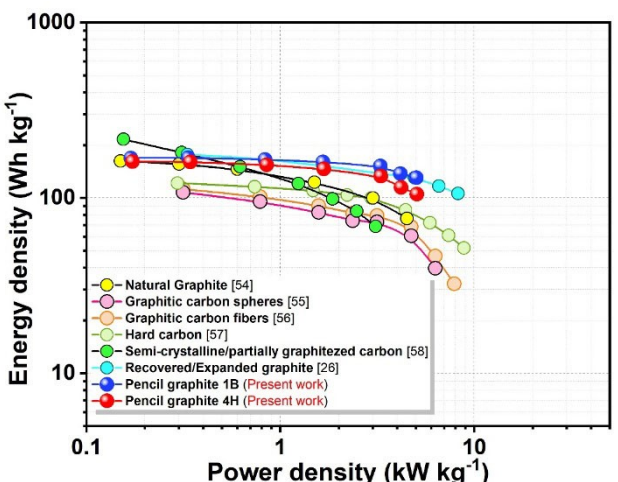


**Figure 6.** Ragone plot comparison of LICs assembled with different graphitic carbon materials paired with AC counter electrode.

(Tester Sangyo, Japan). Disc electrodes of 14 mm diameter were punched out using an electrode cutter. The electrode's approximate mass loading of active material was  $\sim 2\text{-}3 \text{ mg}$ . AC (YP 80F Kuraray, Japan; surface area:  $2100 \text{ m}^2 \text{ g}^{-1}$ , pore volume:  $0.97 \text{ mL g}^{-1}$ ) electrodes were formed by mixing the active material, acetylene black (conductive carbon), and teflonized acetylene black TAB-2 (binder) in the weight ratio 80:10:10 with mortar and pestle using ethanol (solvent) and was pressed on 14 mm diameter stainless steel mesh current collector (Goodfellow, UK). Before cell

assembly, both PG and AC electrodes were vacuum dried for a minimum of 4 h. The coin-cell assembly (CR 2016) of half-cells and full-cells was fabricated in Ar filled glove box. Li metal was considered as the counter/reference electrode in both anode and cathode half-cell assemblies. LIC was made-up of the pre-lithiated-PG electrode as anode and AC as the cathode. 1 M lithium hexafluorophosphate ( $\text{LiPF}_6$ ) in EC: DMC (ethylene carbonate: dimethyl carbonate) 1:1 v/v as electrolyte (Tomiyama, Japan) and Whatman paper (1825-047, GF/F) as separator was used for all the cell assemblies.

### Physicochemical characterization

The crystalline nature and structure of all the PG grades were analyzed by powder X-ray diffraction measurements (XRD, 45 kV @ 200 mA with  $\text{Cu}-K_{\alpha}$  radiation,  $\lambda = 1.5406 \text{ \AA}$ ). Prior to further material characterization, a preliminary electrochemical performance analysis was done to select the suitable PG grades for LIC assembly. Based on the result, PG 1B and PG 4H were chosen in this study for the assembly of LIC and compared their performances. The detailed information about the crystallographic structure, phases, and lattice constants of selected PG grades was analyzed from X-ray diffractogram and Raman spectroscopy (Lab Ram HR800 UV Raman microscope with 515 nm diode laser as excitation light source) measurements. X-ray photoelectron spectroscopy (XPS) was performed to understand the surface chemistry of PG material. The purity and clay content were studied using Energy-dispersive X-ray spectroscopy (EDS) and Thermogravimetric analysis (TGA) (DTG-60H detector). In addition, the morphology and internal structure were scrutinized using field-emission scanning electron

microscopy (FE-SEM), Transmission electron microscopy (TEM), and High-resolution TEM (HR-TEM) images.

### Electrochemical performance analysis

Galvanostatic charge-discharge (GCD), Cyclic voltammogram (CV), and Impedance analysis (EIS) of the fabricated coin-cells were implemented in Battery tester, Battery cycler series (BCS) 805 (Biologic, France). The testing voltage window for Li/PG and Li/AC half-cells were fixed at 0.005–2.00 V vs. Li<sup>+</sup>/Li and 2–4.5 V vs. Li<sup>+</sup>/Li, respectively. Before LIC assembly, the PG electrode was pre-lithiated in half-cell assembly by providing two charge-discharge cycles followed by a final discharge. Further, the PG electrode in pre-lithiated condition was paired with the AC electrode of balanced mass for the LIC fabrication. The energy-power density of assembled LICs was calculated at different current rates. An environmental chamber (Espec, Japan) was used to check the performance of assembled LICs at diverse temperature conditions.

### Acknowledgements

M.L.D. wishes to thank the funding through Women Scientist Scheme-B (DST/WOS-B/2018/2039) from the KIRAN division of the Department of Science & Technology (DST), Govt. of India. Y.S.L. acknowledges the financial support from the National Research Foundation of Korea (NRF) grant funded by the Korean government (Ministry of Science, ICT&Future Planning) (No. 2019R1-A2C1007620). V.A. acknowledges financial support from the Science and Engineering Research Board (SERB), a statutory body of DST, Govt. of India, through Swarnajayanti Fellowship (SB/SJF/2020-21/12).

### Conflict of Interest

The authors declare that they have no known competing interests

### Data Availability Statement

The data that support the findings of this study are available from the corresponding author upon reasonable request.

**Keywords:** anode • energy density • lithium-ion capacitor • pencil graphite • power density • pre-lithiation

- [1] R. Ranjan, Energy Storage is the Way Forward to Meet the Growing Power Demand Through Renewables, 2021. <https://mercomindia.com/energy-storage-power-demand/>.
- [2] A. Z. Al Shaqsi, K. Sopian, A. Al-Hinai, *Energy Rep.* 2020, 6, 288–306.
- [3] E. Hossain, H. M. Faruque, M. S. Sunny, N. Mohammad, N. Nawar, *Energies* 2020, 13.
- [4] D. N. Buckley, C. O'Dwyer, N. Quill, R. P. Lynch, in *Energy Storage Options and Their Environmental Impact*, The Royal Society of Chemistry, 2019, pp. 115–149.
- [5] Y. Zhang, L. Zhang, T. a. Lv, P. K. Chu, K. Huo, *ChemSusChem* 2020, 13, 1114–1154.
- [6] S. Koohi-Fayegh, M. A. Rosen, *J. Energy Storage* 2020, 27, 101047.
- [7] A. Masias, J. Marcicki, W. A. Paxton, *ACS Energy Lett.* 2021, 6, 621–630.
- [8] M. Soltani, S. H. Beheshti, *J. Energy Storage* 2021, 34, 102019.
- [9] A. Jagadale, X. Zhou, R. Xiong, D. P. Dubal, J. Xu, S. Yang, *Energy Storage Mater.* 2019, 19, 314–329.
- [10] B. Li, J. Zheng, H. Zhang, L. Jin, D. Yang, H. Lv, C. Shen, A. Shellikeri, Y. Zheng, R. Gong, *Adv. Mater.* 2018, 30, 1705670.
- [11] M. L. Divya, S. Natarajan, Y. S. Lee, V. Aravindan, *ChemSusChem* 2019, 12, 4353–4382.
- [12] M. L. Divya, V. Aravindan, *Chem. Asian J.* 2019, 14, 4665–4672.
- [13] J. Lamb, O. Burheim, *Energies* 2021, 14, 979.
- [14] T. Huang, Y. Jiang, G. Shen, D. Chen, *ChemSusChem* 2020, 13, 1093–1113.
- [15] Y. An, T. Liu, C. Li, X. Zhang, T. Hu, X. Sun, K. Wang, C. Wang, Y. Ma, *J. Mater. Chem. A* 2021, 9, 15654–15664.
- [16] C. Sun, X. Zhang, C. Li, K. Wang, X. Sun, Y. Ma, *Energy Storage Mater.* 2020, 24, 160–166.
- [17] S. Yi, L. Wang, X. Zhang, C. Li, W. Liu, K. Wang, X. Sun, Y. Xu, Z. Yang, Y. Cao, J. Sun, Y. Ma, *Sci. Bull.* 2021, 66, 914–924.
- [18] R. Kang, W.-Q. Zhu, S. Li, B.-B. Zou, L.-L. Wang, G.-C. Li, X.-H. Liu, D. H. L. Ng, J.-X. Qiu, Y. Zhao, F. Qiao, J.-B. Lian, *Rare Met.* 2021, 40, 2424–2431.
- [19] G. Li, Z. Yang, Z. Yin, H. Guo, Z. Wang, G. Yan, Y. Liu, L. Li, J. Wang, *J. Mater. Chem. A* 2019, 7, 15541–15563.
- [20] X. Wang, L. Liu, Z. Niu, *Mater. Chem. Front.* 2019, 3, 1265–1279.
- [21] S. Saini, P. Chand, A. Joshi, *J. Energy Storage* 2021, 39, 102646.
- [22] H. Zhang, Y. Yang, D. Ren, L. Wang, X. He, *Energy Storage Mater.* 2021, 36, 147–170.
- [23] V. Khomenko, E. Raymundo-Piñero, F. Béguin, *J. Power Sources* 2008, 177, 643–651.
- [24] S. R. Sivakkumar, A. S. Milev, A. G. Pandolfo, *Electrochim. Acta* 2011, 56, 9700–9706.
- [25] M. Cai, X. Sun, W. Chen, Z. Qiu, L. Chen, X. Li, J. Wang, Z. Liu, Y. Nie, *J. Mater. Sci.* 2018, 53, 749–758.
- [26] M. L. Divya, S. Natarajan, Y.-S. Lee, V. Aravindan, *J. Mater. Chem. A* 2020, 8, 4950–4959.
- [27] M. L. Divya, S. Praneetha, Y.-S. Lee, V. Aravindan, *Compos. B. Eng.* 2022, 230, 109487.
- [28] M. C. Sousa, J. W. Buchanan, *Comput. Graph. Forum* 2000, 19, 27–49.
- [29] W.-S. Chang, C.-M. Park, J.-H. Kim, Y.-U. Kim, G. Jeong, H.-J. Sohn, *Energy Environ. Sci.* 2012, 5, 6895–6899.
- [30] H.-Y. Park, M.-S. Kim, T.-S. Bae, J. Yuan, J.-S. Yu, *Langmuir* 2016, 32, 4415–4423.
- [31] R. Navratil, A. Kotzianova, V. Halouzka, T. Opletal, I. Triskova, L. Trnкова, J. Hrbac, *J. Electroanal. Chem.* 2016, 783, 152–160.
- [32] S. Mamidi, A. K. Pandey, A. D. Pathak, T. N. Rao, C. S. Sharma, *J. Alloys Compd.* 2021, 872, 159719.
- [33] S. H. Lee, J. Y. Ban, C.-H. Oh, H.-K. Park, S. Choi, *Sci. Rep.* 2016, 6, 28588.
- [34] A. Ferrari, J. Robertson, S. Reich, C. Thomsen, *Philos. Trans. R. Soc. London Ser. A* 2004, 362, 2271–2288.
- [35] K. Skrzypczyńska, K. Kuśmierk, A. Świątkowski, L. Dąbek, *Int. J. Electrochem. Sci.* 2018, 13, 88–100.
- [36] L. Bokobza, J.-L. Bruneel, M. Couzi, *C* 2015, 1.
- [37] F. Tuinstra, J. L. Koenig, *J. Chem. Phys.* 1970, 53, 1126–1130.
- [38] M. S. Dresselhaus, A. Jorio, A. G. Souza Filho, R. Saito, *Philos. Trans. R. Soc. London Ser. A* 2010, 368, 5355–5377.
- [39] A. Knápek, D. Sobola, D. Burda, A. Daňhel, M. Mousa, V. Kolařík, *Nanomaterials* 2019, 9.
- [40] D. R. Baer, K. Artyushkova, C. R. Brundle, J. E. Castle, M. H. Engelhard, K. J. Gaskell, J. T. Grant, R. T. Haasch, M. R. Linford, C. J. Powell, A. G. Shard, P. M. A. Sherwood, V. S. Smentkowski, *J. Vac. Sci. Technol. A* 2019, 37, 10.1116/1111.505501.
- [41] J. D. Andrade, in *Surface and Interfacial Aspects of Biomedical Polymers: Volume 1 Surface Chemistry and Physics* (Ed.: J. D. Andrade), Springer US, Boston, MA, 1985, pp. 105–195.
- [42] D. J. Morgan, *C J. Carbon. Res.* 2021, 7 (3).
- [43] L. Trnкова, I. Triskova, J. Cechal, Z. Farka, *Electrochim. Commun.* 2021, 126, 107018.
- [44] R. T. Haasch, D. P. Abraham, *Surf. Sci. Spectra* 2020, 27, 014008.
- [45] F. Farivar, P. L. Yap, R. Karunagaran, D. Losic, *C J. Carbon. Res.* 2021, 7, 41.
- [46] C.-W. Lin, Z. Zhao, J. Kim, J. Huang, *Sci. Rep.* 2014, 4, 3812.
- [47] M. Feist, *ChemTexts* 2015, 1, 8.
- [48] L. Cao, J. Huang, Z. Lin, X. Yu, X. Wu, B. Zhang, Y. Zhan, F. Xie, W. Zhang, J. Chen, H. Meng, *J. Mater. Res.* 2018, 33, 1219–1225.
- [49] E. Sivonxay, M. Aykol, K. A. Persson, *Electrochim. Acta* 2020, 331, 135344.

- [50] B. Jerliu, E. Hüger, L. Dörrer, B. K. Seidlhofer, R. Steitz, M. Horisberger, H. Schmidt, *Phys. Chem. Chem. Phys.* **2018**, *20*, 23480–23491.
- [51] Z. Favors, W. Wang, H. H. Bay, Z. Mutlu, K. Ahmed, C. Liu, M. Ozkan, C. S. Ozkan, *Sci. Rep.* **2014**, *4*, 5623.
- [52] S. Chae, S.-H. Choi, N. Kim, J. Sung, J. Cho, *Angew. Chem. Int. Ed.* **2020**, *59*, 110–135; *Angew. Chem.* **2020**, *132*, 112–138.
- [53] B. Li, F. Yao, J. J. Bae, J. Chang, M. R. Zamfir, D. T. Le, D. T. Pham, H. Yue, Y. H. Lee, *Sci. Rep.* **2015**, *5*, 7659.
- [54] P. Sennu, V. Aravindan, M. Ganesan, Y.-G. Lee, Y.-S. Lee, *ChemSusChem* **2016**, *9*, 849–854.
- [55] S. Jayaraman, S. Madhavi, V. Aravindan, *J. Mater. Chem. A* **2018**, *6*, 3242–3248.
- [56] S. Jayaraman, G. Singh, S. Madhavi, V. Aravindan, *Carbon* **2018**, *134*, 9–14.
- [57] S. Jayaraman, A. Jain, M. Ulaganathan, E. Edison, M. P. Srinivasan, R. Balasubramanian, V. Aravindan, S. Madhavi, *Chem. Eng. J.* **2017**, *316*, 506–513.
- [58] P. Sennu, N. Arun, S. Madhavi, V. Aravindan, Y.-S. Lee, *J. Power Sources* **2019**, *414*, 96–102.

Manuscript received: May 10, 2022  
Revised manuscript received: May 24, 2022  
Accepted manuscript online: May 24, 2022  
Version of record online: June 15, 2022